Variable admittance control of the exoskeleton for gait rehabilitation based on a novel strength metric

Ali Taherifar†, Gholamreza Vossoughi†,* and Ali Selk Ghafari‡

†*School of Mechanical Engineering, Sharif University of Technology, Tehran, Iran*
‡*School of Science and Engineering, Sharif University of Technology, International Campus, Kish Island, Iran*

SUMMARY
Assist-as-needed control is underlain by the aim of replacing skillful therapists with rehabilitation robots. The objective of this research was to introduce a smart assist-as-needed control system for the elderly or partially paralyzed individuals. The main function of the proposed system is to assist the patients just in the required sub phases of the motion. To ensure that a smart and compliant system is developed, the target admittance gains of the controller was adapted according to the concept of energy The admittance gains were modified so that an exoskeleton reduces interaction energy in cases wherein users have sufficient strength for task execution and maximizes the interaction energy in the required subphases. The results of simulations and an experimental investigation on a novel exoskeleton showed that the proposed adaptive admittance control improves performance to a level substantially higher than that achieved with constant impedance control.

KEYWORDS: Adaptive admittance control, Exoskeleton, Assist-as-needed control, Human–robot interaction, Strength metric.

1. Introduction
Exoskeletons are used extensively in robotic rehabilitation and power augmentation systems. They can also serve as assistive systems for restoring the gait patterns of partially disabled people and helping the elderly perform daily activities.

During the early development of assistive robotic systems, patients were compelled or guided along a reference trajectory that describes an entire gait pattern.[1] This approach is a passive process, thus driving several researchers to develop impedance-based support devices to enable more active patient participation.[2,3] A recent effort in this regard is the study conducted by Cai *et al.* who investigated the potential of such devices through experimentation with mice; the authors found that spinal injured mice trained with a fixed pattern regained fewer walking abilities than did mice trained with an assist-as-needed (AAN) algorithm.[4]

Taking advantage of the features of an impedance shaping controller, Emken *et al.* introduced a step-by-step learning assistive controller composed of a feedback term that is adjusted at each step.[5] Wolbrecht *et al.* presented an AAN controller based on an adaptive feed-forward term and argued that decreasing assistance during the learning of a new task is necessary to increase the contribution of human muscles to generate the force required to accomplish the task.[6] The authors implicitly assumed that a patient behaves in a similar manner during each repetition of a task, indicating that patient errors always occur in the same locations and directions. This assumption, however, does not always hold. Oboe *et al.* presented a nonlinear adaptive impedance controller based on position errors and adapted the feedback and feed-forward gains of the assistive controller.[7] Their simulation results indicated large impact during high-acceleration phases. In addition, the authors failed to

guarantee the algorithm's stability. Hussain *et al.* put forward an AAN controller that works on the basis of a robust adaptive control approach. The researchers carried out two experiments, namely, a trajectory following experiment and an AAN experiment. However, they did not define any measures for confirming the performance of their algorithm.[8]

As shown in the discussion earlier, advanced control algorithms have been used in developing devices for the rehabilitation of disabled individuals and people suffering from spinal cord injury and stroke. These algorithms, which are usually referred to as AAN controllers, are underlain by the ideal goal of replacing skillful therapists with robotic rehabilitation technologies. The same goal was the main motivation behind the current research, in which an algorithm that brings us a step closer to the ideal goal was developed.

Its objective was to introduce a smart assistive control system that primarily helps elderly or partially paralyzed individuals in the required subphases of the motion while maintaining minimum interaction energy between a human and an exoskeleton. To achieve this objective, an adaptive admittance controller based on a target admittance adaptation law was developed. To validate simulation results, the proposed controller was implemented on a compact, lightweight, powerful, and functional exoskeleton that enables active hip and knee extension/flexion actuation by means of electrical series elastic actuators (SEAs).

The earlier-mentioned features distinguish the current work from previous research in the following manner. Most previous studies[8−12] did not employ the standard form of impedance control, whereas the present study used the standard form of admittance control in the control algorithm and developed a systematic controller design. The controllers proposed in the literature were adapted on the basis of position error; the researchers increased the gains of the controllers in cases wherein position error increased, and gradually decreased the gains over time to increase human participation. These algorithms inadequately cover situations in which a patient has sufficient strength to execute the subphases of gait.

The main novelty of the present study is that unlike previous research, it used the concept of energy, specifically interaction energy, as basis in adapting admittance gains. It also developed a strength metric and incorporated it into the law that governs the adaptation. Using the function approximation technique (FAT), admittance gains and feed-forward force were considered as a function of position (r_1, r_2) and time t.

The rest of the paper is structured as follows. Section 2 describes the establishment of the dynamic model of the swing leg for the augmented human–exoskeleton system. Section 3 focuses on the control scheme for gait rehabilitation and is divided into four subsections. The first subsection presents the block diagram and basic formulation of the admittance control implemented in this work. It also introduces the concept of admittance gains, that is, target admittance. The second subsection details the application of function approximation in reformulating target admittance. The third subsection discusses the novel strength metric developed on the basis of interaction energy. The data derived from the procedures described in the three subsections were used to develop the proposed adaptive admittance controller, which is discussed in the fourth subsection. Section 4 provides the results of two simulations, namely, a simulation on a controller that mimics human functioning and an overall simulation on the augmented human–exoskeleton system. Sections 5 and 6 present the experimental results and the conclusion, respectively.

2. Human–Exoskeleton System: Dynamic Modeling in Cartesian Space

Human–exoskeleton motion in the swing phase was modeled with a double pendulum (Fig. 1) and the effects of hip translational acceleration were also considered. A swing leg model was established to test control performance while avoiding the complexity of modeling an entire body. The mass distribution and geometrical parameter of the model were assumed to be similar to those of a normal human with a weight of 56.7 kg and a height of 170 cm.[13] The physical human properties adopted in this work are indicated in Table I.

The human model and the exoskeleton were assumed to be connected to each other by straps at interaction points, which coincide with the center of mass (Fig. 1). The physical properties of the exoskeleton fabricated in this research are also listed in Table I.

The governing equations of motion for the human and exoskeleton are the same with different physical parameters. The dynamic human–exoskeleton model, which was derived using a Lagrangian

Table I. Physical properties of a normal human (weight $=$ 56.7 kg, height $=$ 170 cm) height and the exoskeleton robot.

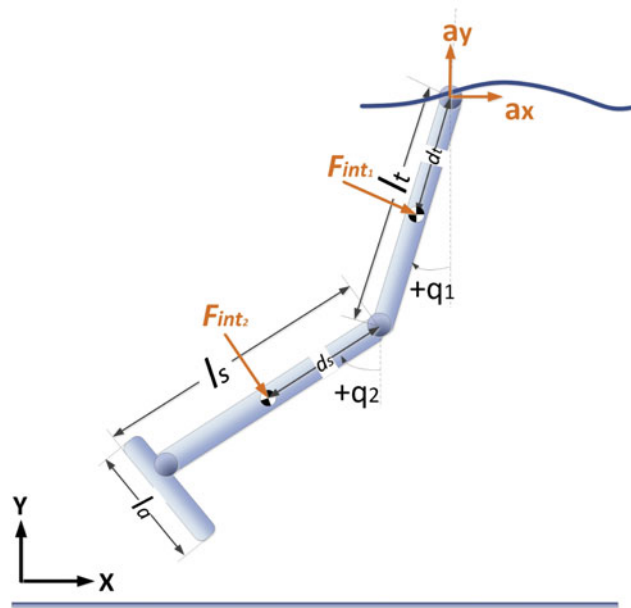| Segment/parameter	Length (m)	Mass (kg)	Moment of inertia (kg·m^2)
Human shank and foot	0.425	2.637	0.042
Human thigh	0.314	5.67	0.103
Exoskeleton shank and foot	0.425	3.5	0.15
Exoskeleton thigh	0.314	5.8	0.22

Fig. 1. Schematic of the exoskeleton model with two active degree of freedom (DoFs) and translational motion of the hip. The direction of the interaction forces is presented.

approach, is expressed as follows:

$$M_r(q_r)\ddot{q}_r + C_r(q_r, \dot{q}_r)\dot{q}_r + G_r(q_r) = B_r\tau_r - J^T F_{\text{int}}$$
$$M_h(q_h)\ddot{q}_h + C_h(q_h, \dot{q}_h)\dot{q}_h + G_h(q_h) = B_r\tau_h + J^T F_{\text{int}}$$

(1)

where subscripts r and h stand for the exoskeleton and the human model, respectively. In this formulation, q denotes the generalized coordinates, $M(q) \in \Re^{n \times n}$ is the symmetric positive definite inertia matrix, $C(q, \dot{q}) \in \Re^n$ denotes the centrifugal and Coriolis vector, $G(q) \in \Re^n$ represents the gravitational effects, $\tau \in \Re^n$ is the vector of the joint torque, and $B \in \Re^{n \times n}$ maps joint torques to limb torques. Limb torques are calculated with the following equation:

$$Q_i = \sum_{j=1:n} \frac{\delta \theta_j}{\delta q_i} \tau_j$$

(2)

where $\theta = [q_1, q_2 - q_1]^T$ represents the relative angles. The limb torques derived in this equation are $Q = [\tau_1 - \tau_2, \tau_2]^T$. In addition, $F_{\text{int}} \in \Re^n$ is the interaction force exerted by the exoskeleton on the human model and $J(q)$ is the Jacobian matrix, defined as,

$$v = J(q)\dot{q}$$

(3)

where v is the linear velocity of the interaction points. The compliant controller was to be derived in the Cartesian space to accommodate task-based rehabilitation programs. This derivation necessitates that the dynamic equation be presented in the Cartesian space as well. The kinematic transformation of joint coordinates into Cartesian coordinates proceeds as follows:

$$
\begin{aligned}
x &= \boldsymbol{\Omega}(q) \\
\dot{x} &= \boldsymbol{J}(q)\dot{q} \\
\ddot{x} &= \boldsymbol{J}(q)\ddot{q} + \dot{\boldsymbol{J}}(q)\dot{q}
\end{aligned}
\tag{4}
$$

where $\boldsymbol{J}(q) = d\boldsymbol{\Omega}(q)/dq$. Equation (1) for non-redundant and non-singular manipulators with a known Jacobian $\boldsymbol{J}(q)$ can be converted from the joint space to the Cartesian space using the following equations:

$$
\begin{aligned}
\boldsymbol{M}_x(x) &= \boldsymbol{J}^{-T}(q)\boldsymbol{M}(q)\boldsymbol{J}^{-1}(q) \\
\boldsymbol{C}_x(x,\dot{x}) &= \boldsymbol{J}^{-T}(q)\left(\boldsymbol{C}(q,\dot{q}) - \boldsymbol{M}(q)\boldsymbol{J}^{-1}(q)\dot{\boldsymbol{J}}(q)\right)\boldsymbol{J}^{-1}(q) \\
\boldsymbol{G}_x(x) &= \boldsymbol{J}^{-T}(q)\boldsymbol{G}(q) \\
\boldsymbol{F}_x(x) &= \boldsymbol{J}^{-T}(q)\tau
\end{aligned}
\tag{5}
$$

With Eqs. (4) and (5), the dynamic equation of the human-exoskeleton system in the Cartesian space can be written as

$$
\boldsymbol{M}_{xr}(x)\ddot{x}_r + \boldsymbol{C}_{xr}(x)\dot{x}_r + \boldsymbol{G}_{xr}(x) = \boldsymbol{F}_r(x) - \boldsymbol{F}_{\text{int}}
\tag{6}
$$

$$
\boldsymbol{M}_{xh}(x)\ddot{x}_h + \boldsymbol{C}_{xh}(x)\dot{x}_h + \boldsymbol{G}_{xh}(x) = \boldsymbol{F}_h(x) + \boldsymbol{F}_{\text{int}}
\tag{7}
$$

where $x_r = x_h = x = [\,r_1\ r_2\,]^T$ is the position vector of the ankle as shown in Fig. 1. The inverse dynamic solution of the presented model was compared with the MATLAB SimMechanics toolbox. A reference position trajectory was assigned to the model, and the joint torques were computed and compared. The inverse dynamic validation test showed that the relative error in the joint torques is limited to less than 10^{-3} N·m.

3. Control Scheme for Gait Rehabilitation

3.1. Basic admittance control

Impedance/admittance control, which was first introduced by Hogan,[14] is the most widely recognized control strategy in research on human–exoskeleton interaction. Impedance control correlates position tracking errors to interaction forces according to a mass–spring–damper relationship. This strategy is implemented through two principal approaches,[15,16] namely, position- and torque-based methods. The present study employed the position-based approach (admittance control).

If the desired values of generalized coordinates are defined as x_d, admittance control can be formulated as follows:

$$
\boldsymbol{M}_d(t)\ddot{\tilde{x}} + \boldsymbol{C}_d(t)\dot{\tilde{x}} + \boldsymbol{K}_d(t)\tilde{x} = \boldsymbol{F}_{\text{int}} - \boldsymbol{F}_d(t)
\tag{8}
$$

where $\boldsymbol{M}_d(t)$, $\boldsymbol{C}_d(t)$, and $\boldsymbol{K}_d(t)$ are the exoskeleton's target inertia, damping, and stiffness matrices in the Cartesian space, respectively. According to the literature of impedance control, the admittance control gains are called target admittance. The performance of admittance controllers depends heavily on environmental dynamics and choice of target admittance.[17] Also, $\boldsymbol{F}_d(t)$ is the feed-forward force and $\ddot{\tilde{x}} = \ddot{x}_d - \ddot{x}_i$, $\dot{\tilde{x}} = \dot{x}_d - \dot{x}_i$, $\tilde{x} = x_d - x_i$. The desired trajectory is a predefined trajectory which is defined according to the normal gait of a healthy human and always contributes to the control system. The target admittance in this study is diagonal matrices; to simplify the calculation, the target
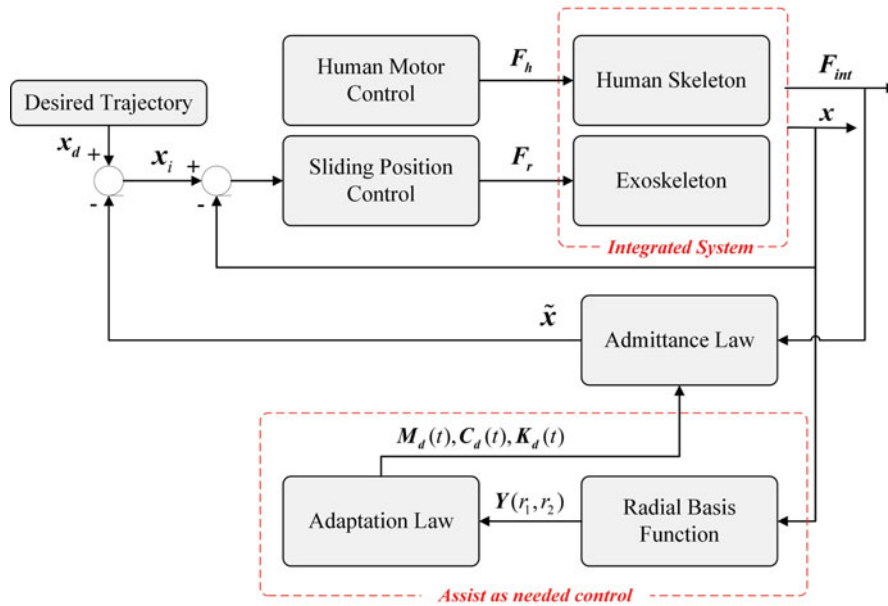
Fig. 2. Block diagram of the proposed adaptive admittance control. The inner loop is the position controller, the middle loop is the admittance controller and the outer loop is the adaptive admittance loop.

admittance vectors are defined as

$$\begin{aligned}
M_d^{\text{vec}} &= \text{diag}(M_d(t)) \\
C_d^{\text{vec}} &= \text{diag}(C_d(t)) \\
K_d^{\text{vec}} &= \text{diag}(K_d(t))
\end{aligned} \tag{9}$$

A block diagram of the proposed assistive-compliant control law is shown in Fig. 2. Note that x_i represents the Cartesian position reference for the inner position control loop as illustrated in Fig. 2. The target impedance matrices were assumed to be positive, time-varying diagonal matrices.

As indicated in Fig. 2, the admittance law is used to calculate $\tilde{x}$, which is subtracted from x_d to calculate x_i. The same procedure is applied for $\dot{\tilde{x}}$, $\dot{x}_d$, $\dot{x}_i$ and second derivatives. The outer loop of the proposed admittance controller takes F_{int} as an input and calculates $\tilde{x}$ and its derivatives according to Eq. (8). The inner position loop takes x_i as a reference and attempts to follow the reference. As in ref. [18], the inner loop uses the sliding surface s and reference trajectory w, and the control law F_r is defined, thus, as

$$\begin{aligned}
e &= x - x_i \\
\dot{e} &= \dot{x} - \dot{x}_i \\
w &= \dot{x}_i - \lambda e \\
\dot{w} &= \ddot{x}_i - \lambda \dot{e} \\
s &= \dot{x} - w \\
\dot{e} &= -\lambda e + s \\
F_r &= M_{xr}\dot{w} + C_{xr}w + G_{xr} - Ks + F_{\text{int}}
\end{aligned} \tag{10}$$

where λ and K are the symmetric, constant, and positive definite gain matrices of position control. The advantages of this method are that the acceleration feedback is not necessary, equations are singularity free and using the regression matrix instead of the detailed dynamic modeling in[19] is easier. This controller allows for the independent stability analysis of inner and outer loops.

In cases wherein exoskeleton parameters M_{xr}, C_{xr}, and G_{xr} are uncertain, the inner loop can be adapted using the technique proposed in.[20]

3.2. Function approximation approach

Admittance control enables the realization of different rehabilitation exercises through modifications to the target admittance gains. In most researches presented in the literature, target admittance was experimentally tuned by trial and error.[21] To the best of our knowledge, little evidence has been found with respect to the target admittance adaptation for the system investigated in the current research. As previously indicated, one of the major contributions of this work is the introduction of an adaptive admittance controller, whose development was facilitated by the adaptation of admittance parameters $M_d(t)$, $C_d(t)$, and $K_d(t)$.

Given that the swing phase involves cyclic motion, admittance gains and feed-forward force must be a functions of position (r_1, r_2) and time t. We used the FAT[22] to realize variations in the admittance gains and feed-forward force as follows:

$$
\begin{aligned}
M_d^{\text{vec}} &= Y(r_1, r_2)b_m(t) \\
C_d^{\text{vec}} &= Y(r_1, r_2)b_c(t) \\
K_d^{\text{vec}} &= Y(r_1, r_2)b_k(t) \\
F_d &= Y(r_1, r_2)b_f(t)
\end{aligned}
\tag{11}
$$

where $Y(r_1, r_2)$ is a $2 \times m$ regression matrix and $b_m(t)$, $b_c(t)$, $b_k(t)$, and $b_f(t)$ are gain vectors. The regressor matrix is composed of dependent Gaussian radial basis functions defined as

$$
\begin{aligned}
Y(r_1, r_2) &= \begin{bmatrix} g^T & 0 \\ 0 & g^T \end{bmatrix} \\
g &= \begin{bmatrix} g_1 & g_2 & \dots & g_{m/2} \end{bmatrix}^T \\
g_i &= \exp\left(-\frac{|r_1 - \mu_{xi}|^2}{2\sigma_x^2} - \frac{|r_2 - \mu_{yi}|^2}{2\sigma_y^2} \right)
\end{aligned}
\tag{12}
$$

where r_1 and r_2 specify the current location of the ankle joint in the x–y plane, μ_x and μ_y are the centers of radial basis functions, and σ_x and σ_y denote the widths of the basis functions. To achieve good function approximation, the function widths (σ_x and σ_y) should be large enough for sufficient overlap between the radial basis functions.

3.3. Strength metric: human contribution to motion

As mentioned earlier, the advanced control algorithms used in rehabilitation are intended to act as skillful therapists. These algorithms are typically called AAN, patient corporative or human-centered algorithms. Their core objectives are to recognize and differentiate the voluntary motions of a patient from the motions that result from disabilities. They are designed to help patients when needed and refrain from intervention when patients are sufficiently strong to execute tasks. In this study, a novel approach was developed to realize assistive control based on interaction force and power.

The diagram shown in Fig. 3 illustrates the different human-exoskeleton interaction states for different levels of human contribution to the motion. The "Human Dynamic" and "Robot Dynamic" columns in the figure pertain to the required dynamic forces for the human model and the exoskeleton in a specific trajectory, respectively. These forces can be determined using the left-hand side of Eqs. (6) and (7).

Figure 3(a) presents a state in which the exoskeleton force is zero and the human force is equal to the sum of the human and exoskeleton dynamics. Because the left-hand side of Eq. (6) is positive, the interaction force must be negative, that is the human moves the exoskeleton. The human contribution to the motion was reduced in Fig. 3(b) and the robot force was increased to satisfy Eqs. (6) and (7). Figure 3(c), shows that the human generates a force equal to his/her dynamics and that the exoskeleton generates only the force equal to that required to move the exoskeleton. Therefore, the interaction force is zero and the human can successfully follow the trajectory. It can be observed that the human contribution is less than his/her dynamics, as shown in Fig. 3(d) and (e), in which case the exoskeleton helps the human. A similar interpretation is presented in Fig. 3(f)–(j). For instance,
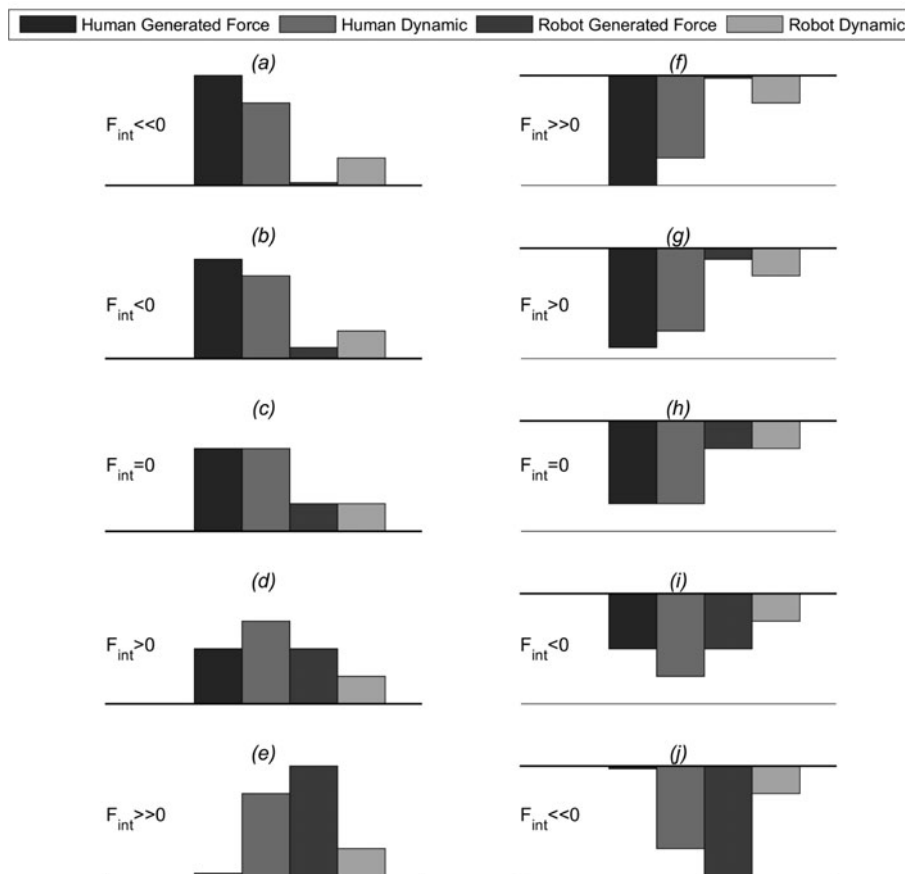
Fig. 3. Human–exoskeleton interaction states for different levels of human contribution to motion (human-generated force).

the human negative force as shown in Fig. 3(f) is equal to the sum of the human and exoskeleton dynamics. Although the human helps the robot in this case, the interaction force is positive.

On the basis of the descriptions above, one can interpret that in the cases shown in Fig. 3(c) and (h), the human is strong enough to follow the trajectory, and strength decreases in the cases shown in Fig. 3(b), (g), (d), and (i). The human can be interpreted as being weak in the cases shown in Fig. 3(a), (f), (e), and (j).

As was described, the human has strength when $\boldsymbol{F}_{\text{int}}$ is small, regardless of whether the human-required dynamic force is positive or negative. According to this fact, a novel strength metric was developed as follows:

$$
\begin{aligned}
S_m &= \frac{\alpha}{\alpha + F_{\text{int}}^2} \\
\alpha &= (z \times \text{Dyn}_h^2)/(1 - z)
\end{aligned}
\tag{13}
$$

where Dyn_h refers to the dynamics of the human (left-hand side of Eq. (7)) and z is a parameter that indicates $0 < z \ll 1$. Figure 4 illustrates the proposed strength metric versus the interaction force. This metric is calculated at each instant of motion.

It can be observed that, as the value of interaction force tends to Dyn_h, the strength metric tends to a small value (z) and the human weakens. By contrast, as interaction force tends to zero, the strength metric tends to 1 and the human becomes stronger.

3.4. Variable admittance formulation
The transferred power, called interaction power, is defined as $\boldsymbol{E}_{\text{int}} = \dot{\boldsymbol{x}}^T \boldsymbol{F}_{\text{int}}$. The positive sign of $\boldsymbol{E}_{\text{int}}$ indicates that the robot transfers energy to the human, whereas the negative sign means that the robot
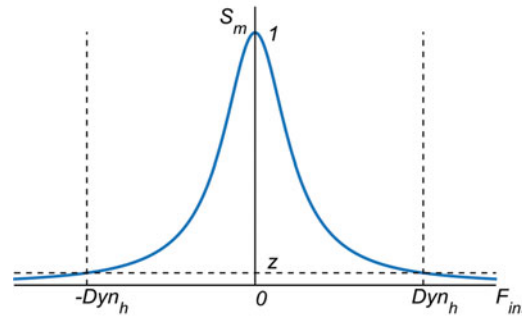
Fig. 4. Proposed strength metric versus interaction force.

receives energy from the human. It should be emphasized that neither the positive nor negative sign of E_{int} indicates that this energy transfer is due to the weakness or strength of the human as illustrated in Fig. 3. However, the strength of the human must be determined according to the human-required dynamic force from Eq. (13).

To formulate the proposed AAN controller, a novel cost function was introduced, and the adaptation laws were derived to minimize the cost function:

$$R = (2S_m - I_v)|E_{int}| \tag{14}$$

where I_v is 2×2 identical matrix and S_m is 2×2 diagonal matrix defined as $S_m = \text{diag}(S_{mx}, S_{my})$ where $S_{mx} = \alpha_x/\alpha_x + F_{\text{int}x}^2$ and α_x are determined in the manner described in the previous subsection. When S_m is small, the human is weak and the robot must supply energy to help the human complete motion. In this case, $|E_{\text{int}}|$ must be increased to minimize the cost function. This means that more energy for transfer to the human is required. When S_m is near one and the human is strong, $|E_{\text{int}}|$ must be reduced because assistance is not required. The objective of the AAN control algorithm is to increase the active participation of a human, that is the exoskeleton should help a patient when required and leave the patient unassisted when the patient has adequate strength for task completion.

The absolute function can be replaced by the Sign function in the following manner:

$$R = (2S_m - I_v)\text{sign}(E_{\text{int}}).E_{\text{int}} \tag{15}$$

The Sign function is then estimated using tanh because it is not a differentiable function. Rewriting the cost function using $E_{\text{int}} = \dot{x}^T F_{\text{int}}$ yields

$$R = \left(\frac{2\alpha}{\alpha + F_{\text{int}}^2} - I_v\right)\tanh(\beta\dot{x}^T F_{\text{int}}).(\dot{x}^T F_{\text{int}}) \tag{16}$$

where β determine the accuracy of approximating Sign with tanh. To determine the adaptation law, the partial derivative of R with respect to $M_{di}, C_{di}, K_{di}, F_{di}\ i = x, y$ must be calculated. Note that $M_{di}, C_{di}, K_{di}, F_{di}$ are the elements of $M_d^{\text{vec}}, C_d^{\text{vec}}, K_d^{\text{vec}}, F_d$ matrices. First, the partial derivative of R_x and R_y with respect to F_{int} in the x and y direction are calculated as follows: (Note that $R = [\ R_x \quad R_y\ ]^T$)

$$
\begin{aligned}
\frac{\partial R_x}{\partial F_{\text{int }x}} &= \frac{-4\alpha_x F_{\text{int }x}}{(\alpha_x + F_{\text{int }x}^2)^2}\tanh(\beta E_{\text{int }x})E_{\text{int }x} + (2S_{mx} - 1)\frac{\beta\dot{r}_1^T}{\cosh^2(\beta E_{\text{int }x})}E_{\text{int }x} \\
&\quad + (2S_{mx} - 1)\tanh(\beta E_{\text{int }x})\dot{r}_1, \\
\frac{\partial R_y}{\partial F_{\text{int }y}} &= \frac{-4\alpha_y F_{\text{int }y}}{(\alpha_y + F_{\text{int }y}^2)^2}\tanh(\beta E_{\text{int }y})E_{\text{int }y} + (2S_{my} - 1)\frac{\beta\dot{r}_2^T}{\cosh^2(\beta E_{\text{int }y})}E_{\text{int }y} \\
&\quad + (2S_{my} - 1)\tanh(\beta E_{\text{int }y})\dot{r}_2
\end{aligned}
\tag{17}
$$

One can use $\boldsymbol{F}_{\text{int}}$ from Eq. (8) to calculate the partial derivative of $\boldsymbol{F}_{\text{int}}$ with respect to $M_{di}, C_{di}, K_{di}, F_{di} \; i = x, y$, thus

$$
\begin{aligned}
\frac{\partial F_{\text{int } x}}{\partial M_{dx}} &= \ddot{\tilde{x}}^T, & \frac{\partial F_{\text{int } y}}{\partial M_{dy}} &= \ddot{\tilde{y}}^T \\
\frac{\partial F_{\text{int } x}}{\partial C_{dx}} &= \dot{\tilde{x}}^T, & \frac{\partial F_{\text{int } y}}{\partial C_{dy}} &= \dot{\tilde{y}}^T \\
\frac{\partial F_{\text{int } x}}{\partial K_{dx}} &= \tilde{x}^T, & \frac{\partial F_{\text{int } y}}{\partial K_{dy}} &= \tilde{y}^T \\
\frac{\partial F_{\text{int } x}}{\partial F_{dx}} &= 1, & \frac{\partial F_{\text{int } y}}{\partial F_{dy}} &= 1
\end{aligned}
\tag{18}
$$

To minimize cost function $\boldsymbol{R}$, the gradient approach is used. The adaptation laws for admittance gains and feed-forward term are proposed as

$$
\begin{aligned}
\dot{\boldsymbol{M}}_d^{\text{vec}} &= -\boldsymbol{\Gamma}_m \left[\begin{array}{cc} \dfrac{\partial R_x}{\partial M_{dx}} & \dfrac{\partial R_y}{\partial M_{dy}} \end{array} \right]^T = \left[\begin{array}{cc} \dfrac{\partial R_x}{\partial F_{\text{int } x}} \dfrac{\partial F_{\text{int } x}}{\partial M_{dx}} & \dfrac{\partial R_y}{\partial F_{\text{int } y}} \dfrac{\partial F_{\text{int } y}}{\partial M_{dy}} \end{array} \right]^T \\
\dot{\boldsymbol{C}}_d^{\text{vec}} &= -\boldsymbol{\Gamma}_c \left[\begin{array}{cc} \dfrac{\partial R_x}{\partial C_{dx}} & \dfrac{\partial R_y}{\partial C_{dy}} \end{array} \right]^T = \left[\begin{array}{cc} \dfrac{\partial R_x}{\partial F_{\text{int } x}} \dfrac{\partial F_{\text{int } x}}{\partial C_{dx}} & \dfrac{\partial R_y}{\partial F_{\text{int} y}} \dfrac{\partial F_{\text{int } y}}{\partial C_{dy}} \end{array} \right]^T \\
\dot{\boldsymbol{K}}_d^{\text{vec}} &= -\boldsymbol{\Gamma}_k \left[\begin{array}{cc} \dfrac{\partial R_x}{\partial K_{dx}} & \dfrac{\partial R_y}{\partial K_{dy}} \end{array} \right]^T = \left[\begin{array}{cc} \dfrac{\partial R_x}{\partial F_{\text{int } x}} \dfrac{\partial F_{\text{int } x}}{\partial K_{dx}} & \dfrac{\partial R_y}{\partial F_{\text{int } y}} \dfrac{\partial F_{\text{int } y}}{\partial K_{dy}} \end{array} \right]^T \\
\dot{\boldsymbol{F}}_d &= -\boldsymbol{\Gamma}_f \left[\begin{array}{cc} \dfrac{\partial R_x}{\partial F_{dx}} & \dfrac{\partial R_y}{\partial F_{dy}} \end{array} \right]^T = \left[\begin{array}{cc} \dfrac{\partial R_x}{\partial F_{\text{int } x}} \dfrac{\partial F_{\text{int } x}}{\partial F_{dx}} & \dfrac{\partial R_y}{\partial F_{\text{int } y}} \dfrac{\partial F_{\text{int } y}}{\partial F_{dy}} \end{array} \right]^T
\end{aligned}
\tag{19}
$$

where the partial derivatives in the first term of this equation can be calculated, for instance, as

$$
\dot{\boldsymbol{M}}_d^{\text{vec}} = -\boldsymbol{\Gamma}_m \left[\begin{array}{c} \left(\begin{array}{c} \dfrac{-4\alpha_x F_{\text{int } x}}{(\alpha_x + F_{\text{int } x}^2)^2} \tanh(\beta E_{\text{int } x}) E_{\text{int } x} \\ + (2S_{mx} - 1) \dfrac{\beta \dot{r}_1^T}{\cosh^2(\beta E_{\text{int } x})} E_{\text{int } x} \\ + (2S_{mx} - 1)\tanh(\beta E_{\text{int } x})\dot{r}_1 \end{array} \right) \ddot{\tilde{x}}^T \\ \\ \times \left(\begin{array}{c} \dfrac{-4\alpha_y F_{\text{int } y}}{(\alpha_y + F_{\text{int } y}^2)^2} \tanh(\beta E_{\text{int } y}) E_{\text{int } y} \\ + (2S_{my} - 1) \dfrac{\beta \dot{r}_2^T}{\cosh^2(\beta E_{\text{int } y})} E_{\text{int } y} \\ + (2S_{my} - 1)\tanh(\beta E_{\text{int } y})\dot{r}_2 \end{array} \right) \ddot{\tilde{y}}^T \end{array} \right]^T
$$

The other terms in Eq. (19) can be determined in the similar manner. In this equation, $\boldsymbol{\Gamma}_m, \boldsymbol{\Gamma}_c, \boldsymbol{\Gamma}_k$, and $\boldsymbol{\Gamma}_f$ are positive, and constant 2×2 adaptation rate matrices. Substituting the definition of admittance parameters (Eq. (11)) into Eq. (19) and using the pseudo inverse of $\boldsymbol{Y}$ yields

$$
\begin{aligned}
\dot{\boldsymbol{b}}_m(t) &= \boldsymbol{Y}^T (\boldsymbol{Y}\boldsymbol{Y}^T)^{-1} \dot{\boldsymbol{M}}_d^{\text{vec}} \\
\dot{\boldsymbol{b}}_c(t) &= \boldsymbol{Y}^T (\boldsymbol{Y}\boldsymbol{Y}^T)^{-1} \dot{\boldsymbol{C}}_d^{\text{vec}} \\
\dot{\boldsymbol{b}}_k(t) &= \boldsymbol{Y}^T (\boldsymbol{Y}\boldsymbol{Y}^T)^{-1} \dot{\boldsymbol{K}}_d^{\text{vec}} \\
\dot{\boldsymbol{b}}_f(t) &= \boldsymbol{Y}^T (\boldsymbol{Y}\boldsymbol{Y}^T)^{-1} \dot{\boldsymbol{F}}_d^{\text{vec}}
\end{aligned}
\tag{20}
$$

To simulate the proposed controller, differential Eqs. (8), (10), (19), and (20) and dynamic Eqs. (6) and (7) were numerically solved. The differential equations were calculated using the "ode45" algorithm. The numerical calculation of the terms in Eq. (19) was not a concern since all the variables were determined previously as was presented for $\dot{\boldsymbol{M}}_d^{\text{vec}}$.

4. Simulation Study

4.1. Human controller simulation

Thus far, the dynamic model of the augmented human skeletal and exoskeleton structure has been derived, and an impedance controller for the exoskeleton has been proposed. If the human is assumed to be completely paralyzed, the passive torque of muscles can be examined, and the human–exoskeleton model can be simulated using Eq. (1). For a healthy, weak, or partially paralyzed human, however, the central nervous system of the human must be modeled and simulated.

As the neural system of humans is highly complicated and that several of its aspects are remain unknown, no complete and verified model of the human motor control has been presented in the literature. In the current work, one of the more widely accepted controllers that mimic the human neural system in the swing phase is used. This model was first introduced by Geyer[23,24] and later integrated with the famous neuromusculoskeletal model.[25] The main features of the model are as follows:

1. No predefined trajectory is established for the joints.
2. It is robust to external disturbances.
3. The dynamics of the pendulum motion of the knee is considered in the controller.
4. Local feedback is used in a similar manner as human biological feedback.

This model has been validated with the following evidences:

1. The ankle trajectory in the x–y plane matches the real trajectory of the human.
2. The trend of joint torques closely follows the trend observed in experiment.
3. The model is robust to initial joint angle and velocity.

4.2. Simulation results

A repetitive swing leg motion was simulated for the human–exoskeleton system. The desired trajectory of the exoskeleton (x_d) was adopted from the normal gait of a healthy human.[13] The step length was 0.7 m, and the walking speed was about 0.71 m/s. The gains of the human swing leg controller (HSLC), the gains of the inner position loop control and the gains of the adaptive admittance control for this simulation are shown in Table II.

The simulation was performed for three general cases. In the first case, the human can actively participate for a certain period of motion. In the second case, the human is healthy, and the human torques resulting from muscle activation are calculated from HSLC.[23] In the third case, the human is assumed to be completely paralyzed and all human joint torques are zero. The results showed that the proposed algorithm reduce the cost function in any possible scenario of human behavior.

In the simulation, 10 grid divisions each in the x (0.05, 1.6)m and y (0.05, 0.4)m directions were established, leaving us with 100 basis functions ($m = 200$). The dimensions of the regressor matrix were 2 × 200. The values of σ_x and σ_y were 0.065 and 0.016 m in the x and y directions, respectively.

Four indices were defined to examine the performance of the proposed algorithm. These indices were evaluated in the x and y directions and in relation to the sum of the directions.

$$
\begin{aligned}
J_{1i} &= \sqrt{\frac{\sum \boldsymbol{E}_i^T \boldsymbol{E}_i}{N}}, \\
J_{2i} &= \sqrt{\frac{\sum \boldsymbol{F}_{\text{int}_i}^T \boldsymbol{F}_{\text{int}_i}^T}{N}}, \\
J_{3i} &= \sqrt{\frac{\sum (\max(0, \boldsymbol{R}_i))^T (\max(0, \boldsymbol{R}_i))}{N}} \\
J_{4i} &= \sqrt{\frac{\sum (\min(0, \boldsymbol{R}_i))^T (\min(0, \boldsymbol{R}_i))}{N}}, \qquad i = x, y
\end{aligned}
\tag{21}
$$

In the equation above, $\boldsymbol{E}$ and $\boldsymbol{J}$ are the position error vector and cost function, respectively, and N denotes the size of the vectors. The first index indicates the Root Mean Square (RMS) position error. Position error is the difference between the desired trajectory (x_d) and the actual trajectory (x).

Table II. Gains of the human swing leg controller, inner position loop control, and adaptive admittance control.

			Human swing leg control (HSLC)					
K_P^α	K_d^α	K^i	K^{ii}	K_{stp}	K^{ext}	$\dot{\alpha}_{max}$	α_{tgt}	α_{thr}
20	4	20	5.5	200	200	10	70	74

Inner position loop control	
K	λ
$200I_{2\times2}$	$10I_{2\times2}$

Adaptive admittance control	
$\boldsymbol{\Gamma}_m$	$\boldsymbol{\Gamma}_c$
$2 \times 10^2 \text{diag}([\ I_{100\times100}\ \ I_{100\times100}\ ])$	$15 \times 10^4 \text{diag}([\ I_{100\times100}\ \ I_{100\times100}\ ])$
$\boldsymbol{\Gamma}_k$	$\boldsymbol{\Gamma}_f$
$6 \times 10^5 \text{diag}([\ 5I_{100\times100}\ \ 4I_{100\times100}\ ])$	$60 \text{diag}([\ I_{100\times100}\ \ 4I_{100\times100}\ ])$
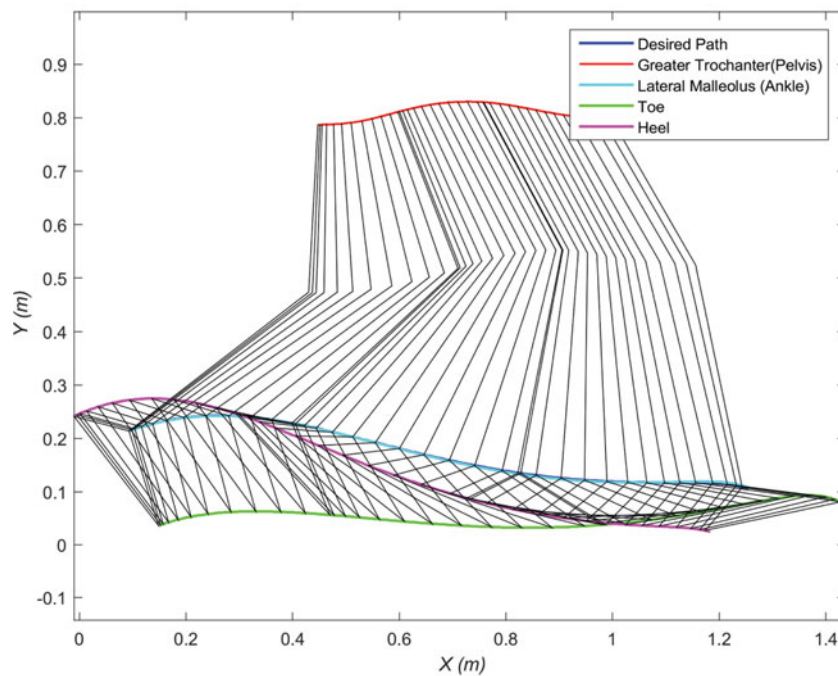
Fig. 5. Simulated motion path of the human–exoskeleton system.

The second index calculates the RMS interaction force and the third and fourth indices determine the RMS of the Positive Part of the Cost Function (PPCF) and the Negative Part of the Cost Function (NPCF), respectively.

For the first case (partially active human), the motion path of the augmented human–exoskeleton in the swing phase of motion is shown in Fig. 5. The swing phase of motion is a single support phase that starts with toe off and ends with heel contact. Without loss of generality, hip translational motion instead of human leg stance was considered in the simulation, as stated in Section 2.

Figure 6(f) shows that the human exerts a linearly increasing force in [0.17 0.30] s in the *y* direction, thereby causing the interaction force to decrease to a level below 0 and the strength metric to tend to 1 (Fig. 6(h)).

The linear velocity of the leg in different cycles is indicated in Fig. 6(a) and (e). The linear velocity in the *x* direction is positive, except in the last 0.08 s of motion, which is an acceptable result for the swing phase of gait. The interaction-induced exoskeleton and human force and the force in the hip and knee joints are illustrated in Fig. 6(b) and (f). The cost functions in the x and y directions are
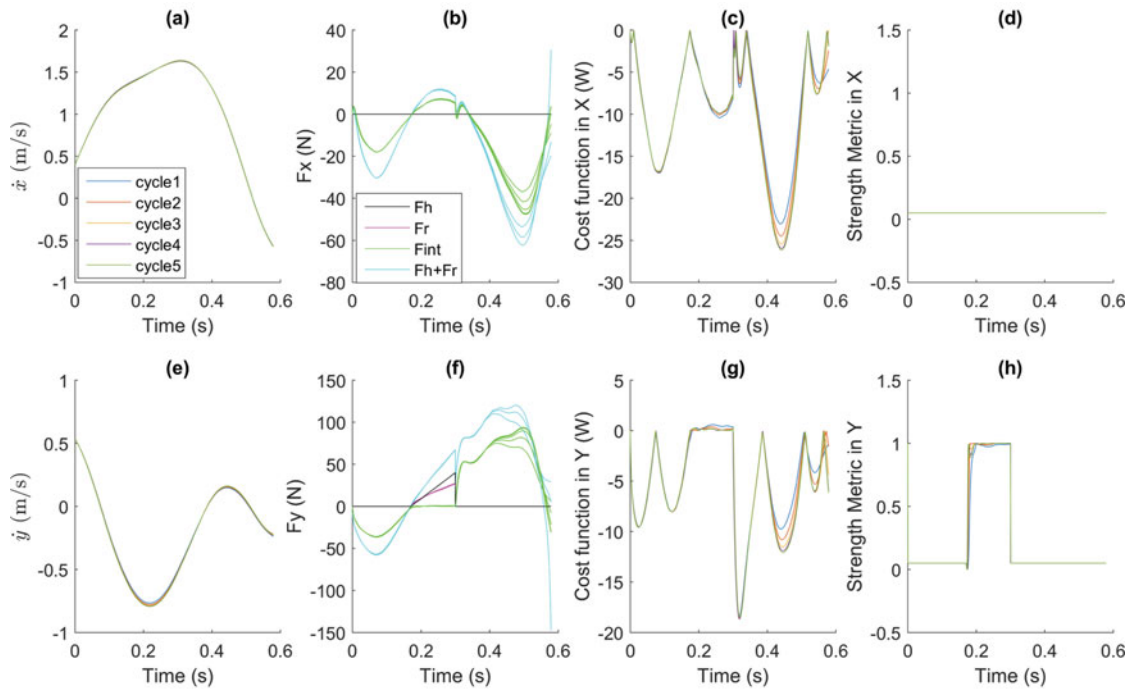
Fig. 6. (a) Leg linear velocity in X, (b) leg force in X direction, (c) cost function in X, (d) strength metric in X, (e) leg linear velocity in Y, (f) leg force in Y direction, (g) cost function in Y, (h) strength metric in Y direction. Representations are for five continuous cycles in the case wherein the human is partially active.
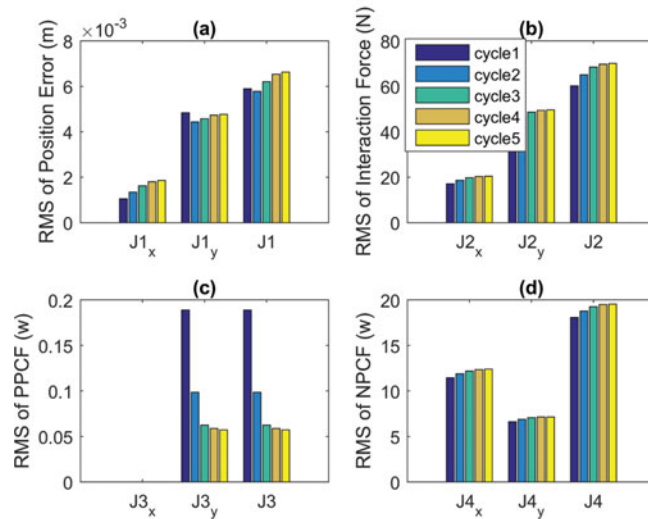

Fig. 7. Comparison of different indices in five continuous cycles in the x and y directions in the case wherein the human is partially active. The first and second columns in each chart indicates the values of the indices in the x and y directions, respectively, and the third column is the sum of the indices in the both directions. (a) First index—J_1, (b) second index—J_2, (c) third index—J_3, (d) fourth index—J_4.

shown in Fig. 6(c) and (g), respectively. These figures also show that the cost function is positive. At [0.3 0.6] s, the strength metric is positive, and the cost function is negative.

The bar chart presented in Fig. 7 displays the position, force, and energy indices in five continuous swing cycles. The NPCF increases in the x and y directions, whereas the PPCF decreases. The figure indicates that the proposed adaptation law (i.e., Eq. (20)) successfully reduces the cost function in Eq. (6) in five cycles. This success is ascribed to the decrease and increase in the positive and negative parts of the cost function, respectively.
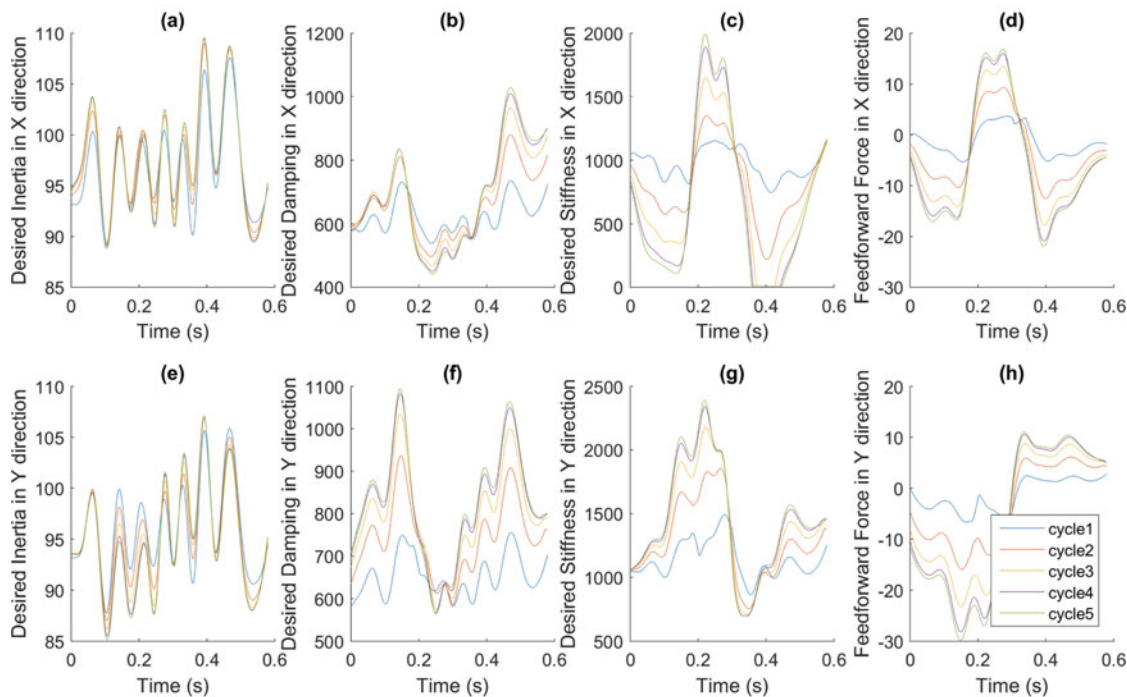
Fig. 8. (a) Desired inertia in X direction, (b) desired damping X direction, (c) desired stiffness X direction, (d) feed forward in X direction, (e) desired inertia in Y direction, (f) desired damping Y direction, (g) desired stiffness Y direction, (g) feed forward in Y direction, (h) feed forward in Y direction. Representations are for five continuous cycles in the case wherein the human is partially active.

Figure 8 shows the admittance gains and feed-forward force during the gait cycles. The inertia, damping, and stiffness coefficient in the x and y direction were changed according to Eq. (20). It can be observed that all the gains converge into a certain value in both the x and y directions, indicating that the adaptation law is stable. The desired inertia is gradually changed due to low adaptation learning gains.

The value of the feed-forward term in the x direction was adapted on the basis of the values of $\partial F_{\text{int } i}/\partial F_{di}$ and $\partial R_i/\partial F_{\text{int } i}$ (Fig. 8(d)). Given that the first term is equal to 1, the second term is highly positive and negative at 0.17 and 0.35 s, respectively. It also causes a sudden change in $\dot{b}_{fx}(t)$. As shown in Fig. 8(c), stiffness suddenly varies in the x direction because of the change in the sign of the interaction force (Fig. 6(b)).

The admittance gains and feed-forward force in the Cartesian plane (x–y plane) are presented in Fig. 9, which also depicts the admittance gain surface and feed-forward surface in the last cycle. This figure is the same as Fig. 8, except that the output is illustrated versus the x–y coordinate rather than time

In the case where the human is healthy, the strength metric is positive at a certain duration of gait (Fig. 10). The proposed method functions perfectly, as demonstrated in Fig. 11. Compared with the NPCF in the partially active case, that in the healthy case increases in magnitude because the human neural control system acts against the robot at a certain duration of the cycle. As observed in Fig. 10(b) and (f), the human torque in the hip joint is negative at the beginning of swing motion, thereby increasing the hip angle; it is positive at the end of motion, thereby enabling deceleration. The knee joint torque is positive at the beginning, thus enabling the flexing of the knee joint and the avoidance of foot contact with the ground. Furthermore, the interaction and robot torques only slightly differ because of the small torque required to overcome the robot dynamics.

The trend of human torque in the hip and knee joint in the healthy human case is the same as that reported in the literature.[13] This confirms that the controller intended for human action functions effectively.

The results on the case wherein the human is completely passive are presented in Figs. 12 and 13. Because the human is completely passive, the human torque is 0, and the interaction torque is almost
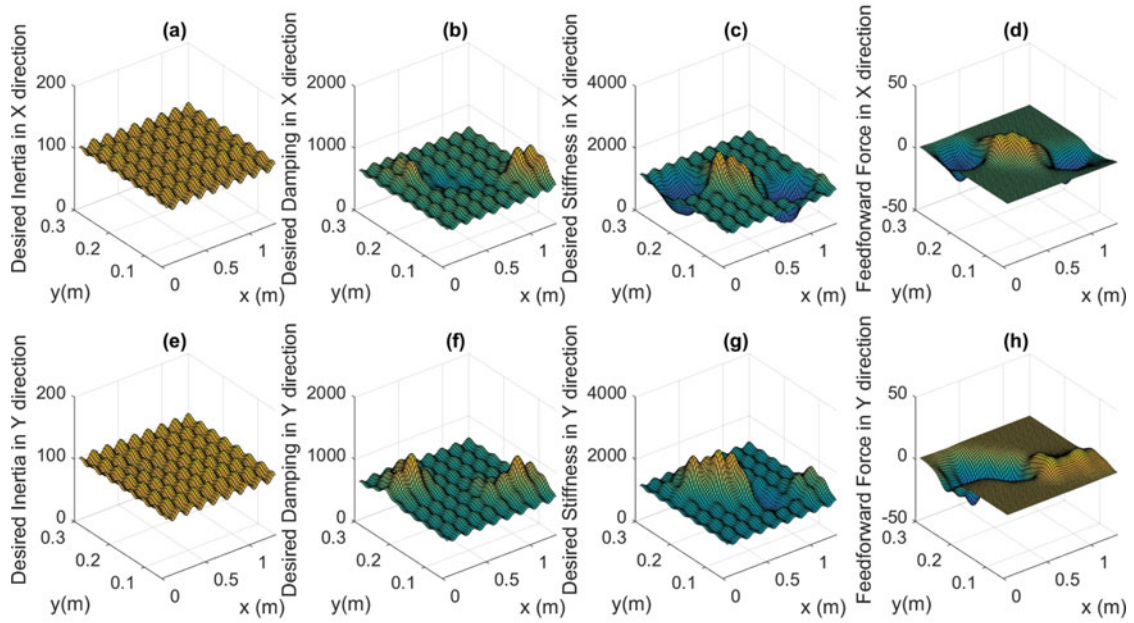
Fig. 9. Final values of admittance gains and feed-forward force in the $x-y$ plane after five cycles in the case where the human is partially active.
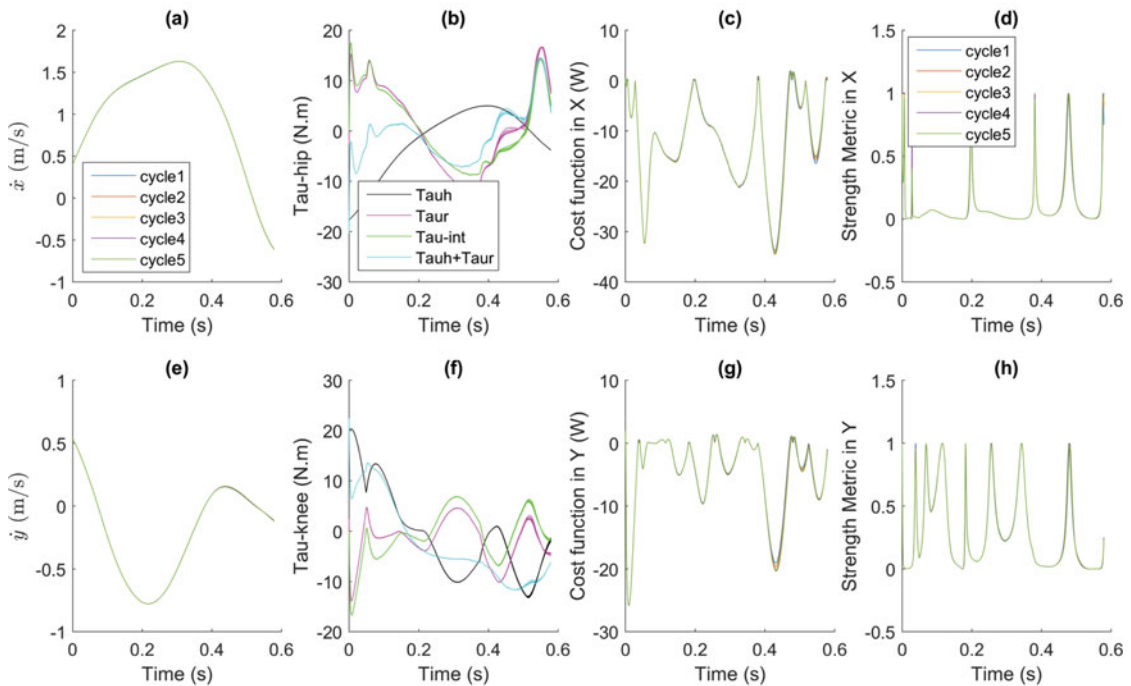

Fig. 10. (a) Leg linear velocity in X, (b) leg force in X direction, (c) cost function in X, (d) strength metric in X, (e) leg linear velocity in Y, (f) leg force in Y direction, (g) cost function in Y, (h) strength metric in Y direction. Representations are for five continuous cycles in the case wherein the case that the human is healthy.

equal to that of the robot (Fig. 12(b) and (f)). As the robot inertia decreases, the difference between the interaction and robot torques also declines.

The cost function is mostly negative and increases in magnitude during the cycles, indicating that the human has insufficient strength in this case (Fig. 12(c) and (g)). The strength metrics in the x and y directions are presented in Fig. 12(d) and (h); for these directions, the strength metric was calculated using Eq. (13). In this simulation, the human joint torques were set to 0, and the proposed strength
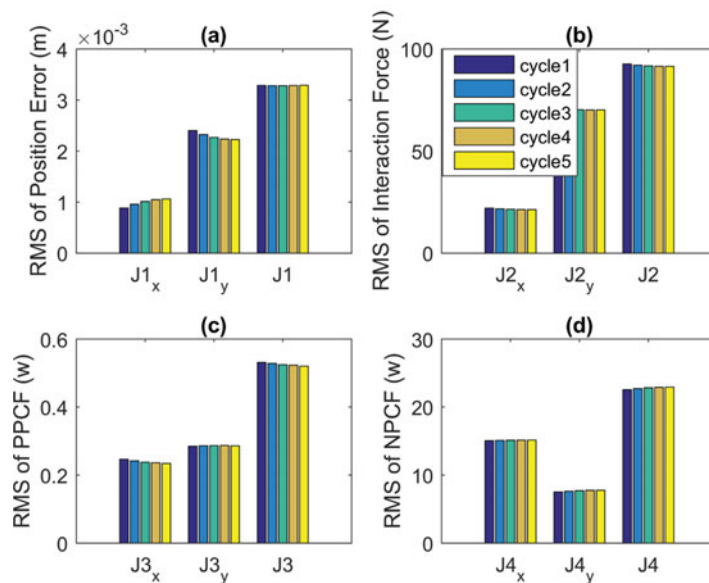
Fig. 11. Comparison of different indices in five continuous cycles in the *x* and *y* directions in the case wherein the human is healthy. The first and second columns in each chart indicates the values of the indices in the *x* and *y* directions, respectively and the third column is the sum of the index in the both directions. (a) First index—J_1, (b) second index—J_2, (c) third index—J_3, (d) fourth index—J_4.
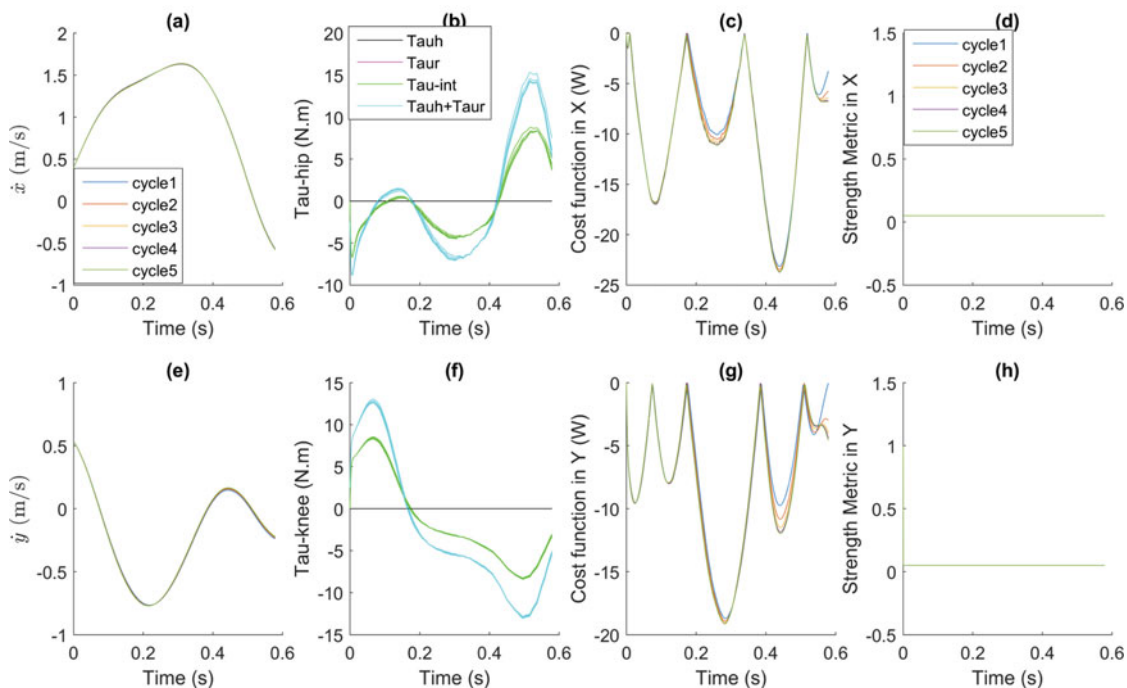

Fig. 12. (a) Leg linear velocity in *X*, (b) leg force in *X* direction, (c) cost function in *X*, (d) strength metric in *X*, (e) leg linear velocity in *Y*, (f) leg force in *Y* direction, (g) cost function in *Y*, (h) strength metric in *Y* direction. Representations are for five continuous cycles in the case wherein the human is completely passive.

metric was calculated as 0. These confirm that the human in the scenario is paralyzed. The third and fourth metrics shown in Fig. 13 reflect substantial improvement in performance during the cycles.

To verify the performance of the proposed algorithm, the constant target impedance and the developed adaptive impedance control were compared. Five sets of impedance gains (Table III) were selected for the comparison.

Table III. Five sets of constant target impedance.

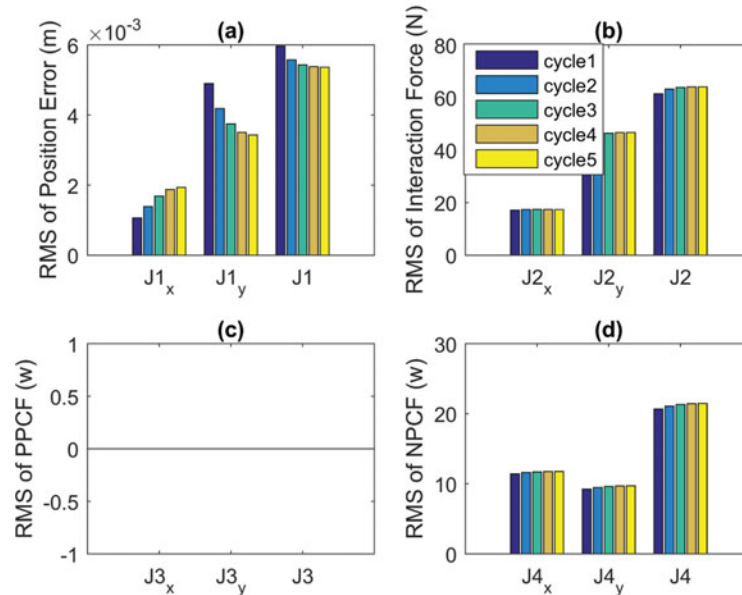| Target impedance	SET 1	SET 2	SET 3	SET 4	SET 5
ω_n	8	16	24	32	40
$\boldsymbol{M}_d^{\text{vec}}$	50[1,1]	130[1,1]	210[1,1]	290[1,1]	370[1,1]

Fig. 13. Comparison of different indices in five continuous cycles in the x and y directions in the case wherein the human is completely passive. The first and second columns in each chart indicate the values of the indices in the x and y directions, respectively and the third column is the sum of the index in the both directions. (a) First index—J_1, (b) second index—J_2, (c) third index—J_3, (d) fourth index—J_4.

where $\boldsymbol{K}_d^{\text{vec}} = \boldsymbol{M}_d^{\text{vec}}\omega_n^2$, $\boldsymbol{C}_d^{\text{vec}} = 2\xi\sqrt{\boldsymbol{M}_d^{\text{vec}}\boldsymbol{K}_d^{\text{vec}}}$, and ξ is supposed to be 1 in all the impedance gain sets. The ith cycle was assumed to be completed with the ith set of the target impedance gains. Figure 14 presents the results of the five cycles. Increasing the target impedance does not necessarily decrease the NPCF or increase the PPCF. In contrast to the proposed algorithm, the AAN controller cannot be realized using constant target impedance.

5. Experimental Validation

An experimental test was performed to validate the appropriate performance of the proposed adaptive admittance controller. To examine the controller, a lower limb exoskeleton that uses SEAs was designed and constructed (Fig. 15). The experimental test was executed on 1-DoF joint (hip joints of the exoskeleton), and the other joints were disassembled.

The exoskeleton frame is constructed from aluminum tubes (black tubes). Two rounded frame was also designed for the thigh and shank part of the robot (purple element). This rounded frame supports the culfs which are made of polyethylene (white element). The culfs are attached to the human leg with straps (black belts). Through this arrangement, the exoskeleton is attached to the human leg. The human foot is also attached to the exoskeleton foot with straps.

For data collection, a data acquisition card that receives data from the force sensor and joint incremental encoder was used. The precision of analogue-to-digital conversion of the DAQ is 16 bits. Desired analog velocity commands are sent to motor drivers, and position is read via a USB port. A force sensor with a capacity of 20 kgf is used in the straps. The resolution of the joint encoder is 10,000 pulses per revolution, which is equal to 40,000 quadrature states per revolution, thus providing sufficient precision for position control. All the received data are transmitted into a computer through a high-speed USB port at a rate of 200 Hz.
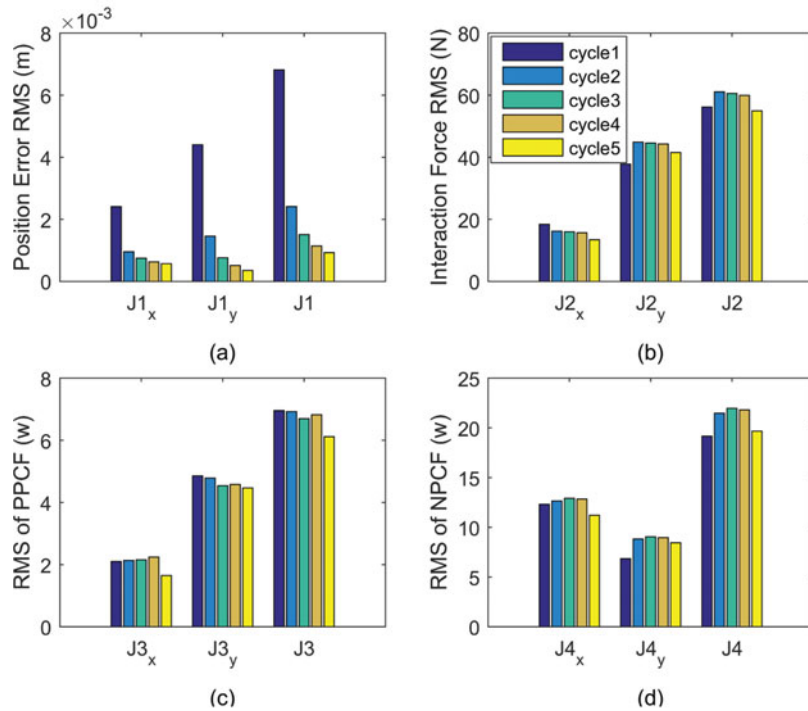
Fig. 14. Comparison of different indices in five set of constant impedance gain in the x and y directions in the case wherein human is partially active. The first and second columns in each chart indicate the values of the indices in the x and y directions, respectively, and the third column is the sum of the index in the both directions. (a) First index-J_1, (b) Second index-J_2, (c) Third index-J_3, (d) Fourth index-J_4.
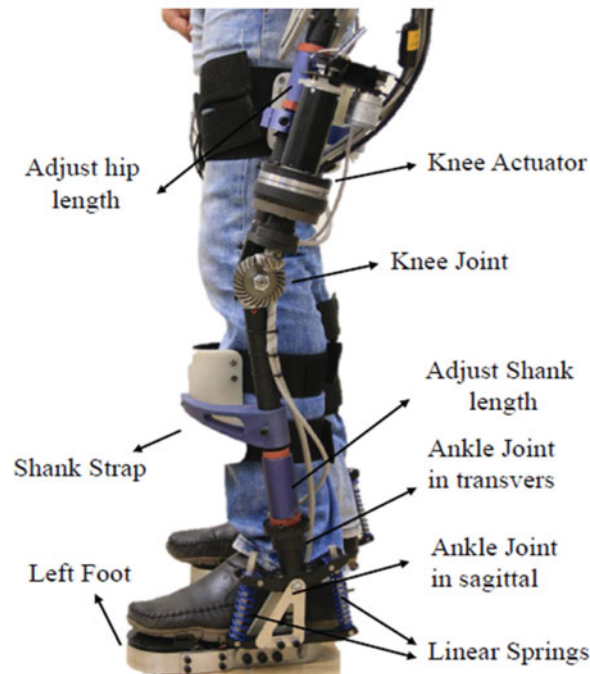

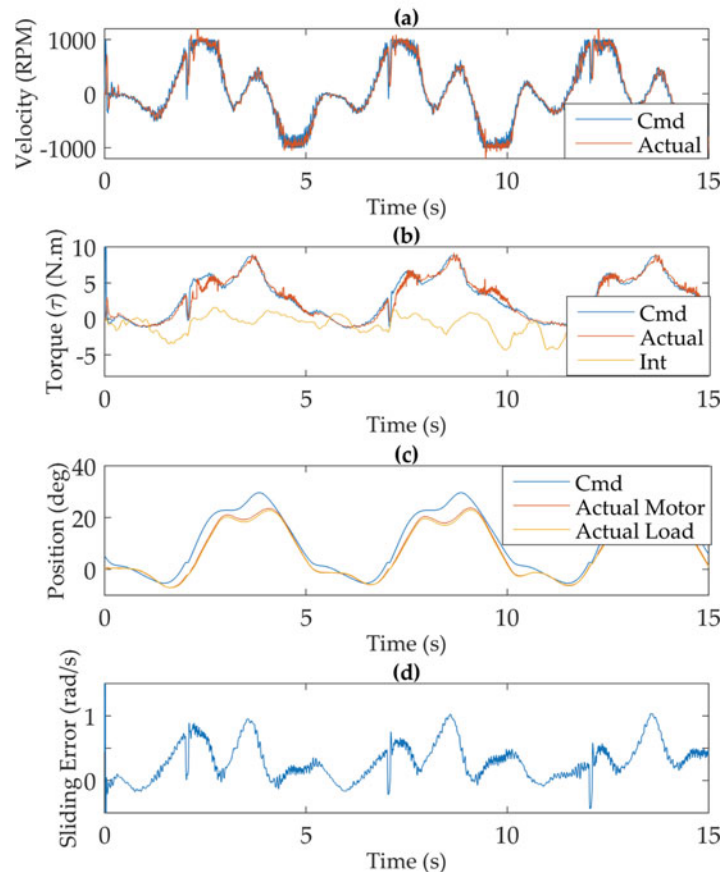Fig. 15. Prototype of the lower limb exoskeleton used in the experimental test.

Fig. 16. (a) The velocity, (b) torque, (c) position and (d) sliding error of the hip joint in the experimental test.

The experimental test was conducted on a healthy subject, who was asked to repeat the swing motion as he was attached to the exoskeleton. The velocity, torque, position, and sliding error in the hip joint are shown in Fig. 16. The command and actual velocity in the hip motor coincide well with each other (Fig. 16(a)). The oscillation of the actual velocity is due to the derivation of the encoder output. The torque tracking in the hip joint is indicated in Fig. 16(b). The actual torque was measured on the basis of series elastic spring deflection. Because the human is healthy, a small torque is transferred to the human, generating a torque less than 9 Nm. The desired position, the actual position of the motor, and the load imposed on the hip joint are depicted in Fig. 16(c). The actual position of the motor slightly differs from that of the load because of spring deflection. This difference is directly related to the actual torque by the spring stiffness law. The implementation of admittance control generates a difference between the desired and actual positions. The sliding error shown in Fig. 16(d) is less than 1 rad/s.

The target stiffness and damping are shown in Fig. 17. The target stiffness increases at 2–3 s because the subject could not follow the desired trajectory in this period (Fig. 16(c)). As a result, the interaction energy and the target stiffness and damping increase, thereby enabling AAN control. The target stiffness and damping gradually increase because of the low learning rates.

Qualifying and validating the advantages of an AAN controller necessitate the definition of quantitative metrics. In this research, a novel cost function (R) that must be minimized was defined. This cost function is a function of interaction energy. When R decreases during motion cycles, the assistance force in the required subphases of motion increases. In the simulation and experimental sections, the magnitude of R in different cycles of motion is presented to demonstrate the advantage of the proposed method.

Figure 18 shows the four indices presented in Eq. (21) for the hip joint in the experimental test. The sliding error decreases in different cycles (Fig. 18(a)) because of the increase in the admittance gains. Furthermore, the RMS of the NPCF increases in the hip joint, reflecting the performance of
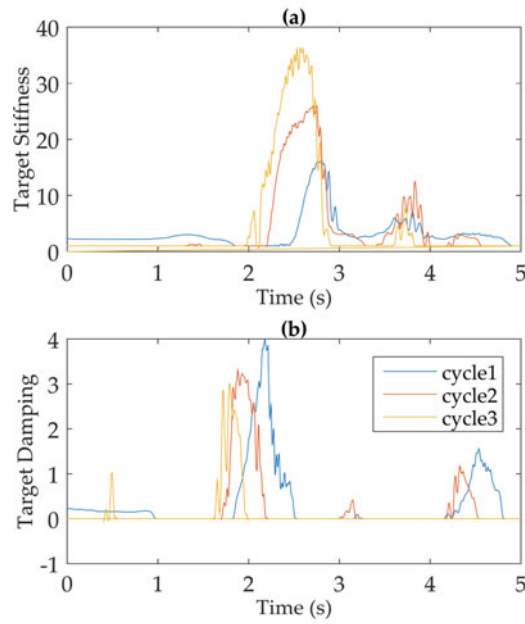
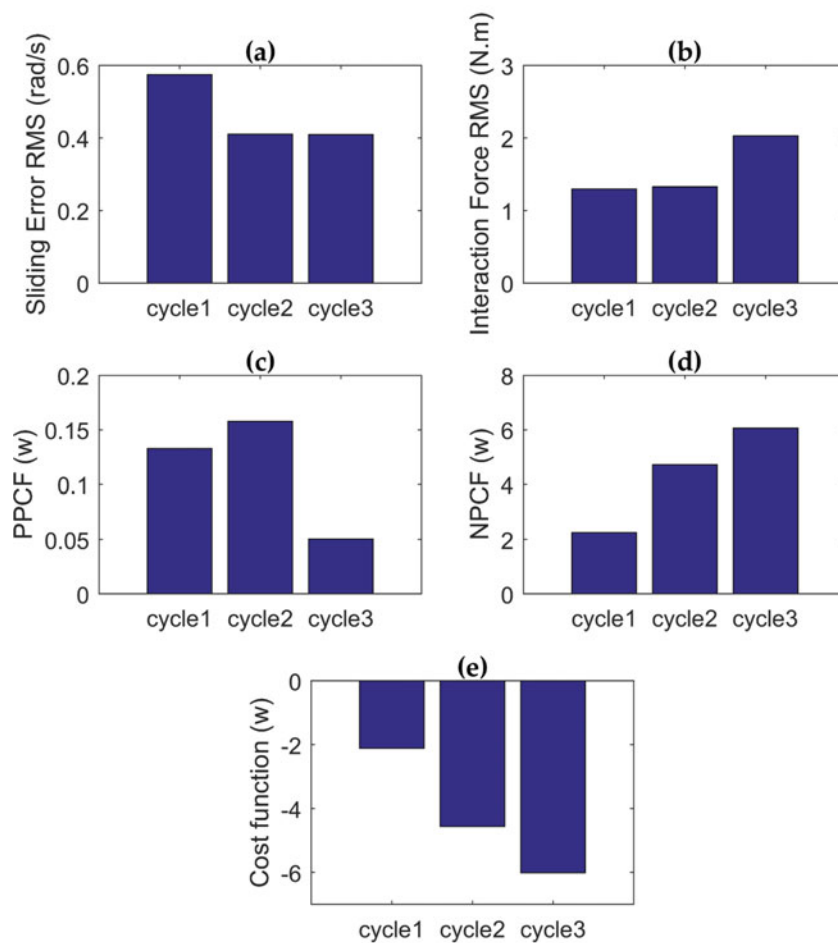Fig. 17. (a) Target stiffness and (b) damping in the experimental test.

Fig. 18. Comparison of different indices in three continuous cycles in the experimental test. The first and second columns in each chart indicates the values of the indices in hip and knee joints. (a) First index—J_1, (b) second index—J_2, (c) third index—J_3, (d) fourth index—J_4, (e) cost function.

the introduced adaptation law. The PPCF slightly increases in Cycle 2 but decreases in Cycle 3. This finding is attributed to human muscle adaptation or fatigue, which was not considered in this research. Figure 18(e) illustrates the adaptation law's cost function, which decreases during the motion cycles. According to the definition of the cost function (Eq. (14)), when the cost function decreases, AAN control increases. Consequently, the energy required in such control rises during the experimental test.

6. Conclusions
A smart–compliant assistive control system was developed on the basis of energy and power. An adaptive admittance controller was designed according to a novel cost function. When the cost function is minimized, interaction power changes in accordance with human strength in different gait cycles. Interaction power increases when the strength metric is low, indicating that an exoskeleton is helping a human in a certain subphase of motion. Conversely, interaction power decreases according to the proposed adaptation law when the strength metric is high, reflecting that a human is strong enough to independently execute motion. The human neural control system was simulated by an advanced robust controller. The proposed algorithm was verified in an experiment and three simulation cases of healthy, paralyzed, and partially paralyzed humans.

References
1. R. Riener, L. Lunenburger, S. Jezernik, M. Anderschitz, G. Colombo and V. Dietz, "Patient-cooperative strategies for robot-aided treadmill training: first experimental results," *IEEE Trans. Neural Syst. Rehabil. Eng.* **13**(3), 380–394 (2005).
2. J. L. Emken, J. E. Bobrow and D. J. Reinkensmeyer, "Robotic Movement Training as an Optimization Problem: Designing a Controller that Assists only as Needed," Proceedings of the Rehabilitation Robotics, 2005. ICORR 2005. 9th International Conference on *IEEE* (2005) pp. 307–312.
3. Y. Han, S. Zhu, Z. Zhou, Y. Shi and D. Hao, "Research on a multimodal actuator-oriented power-assisted knee exoskeleton," *Robotica* **35**(9), 1906–1922 (2016).
4. L. L. Cai et al., "Implications of assist-as-needed robotic step training after a complete spinal cord injury on intrinsic strategies of motor learning," *J. Neuroscience* **26**(41), 10564–10568 (2006).
5. J. L. Emken, S. J. Harkema, J. Beres-Jones, C. K. Ferreira and D. J. Reinkensmeyer, "Feasibility of manual teach-and-replay and continuous impedance shaping for robotic locomotor training following spinal cord injury," *IEEE Trans. Biomed. Eng.* **55**(1), 322–334 (2008).
6. E. T. Wolbrecht, V. Chan, D. J. Reinkensmeyer and J. E. Bobrow, "Optimizing compliant, model-based robotic assistance to promote neurorehabilitation," *IEEE Trans. Neural Syst. Rehabil. Eng.* **16**(3), 286–297 (2008).
7. R. Oboe and D. Pilastro, "Non-linear Adaptive Impedance Controller for Rehabilitation Purposes," *Proceedings of the Advanced Motion Control (AMC), 2014 IEEE 13th International Workshop on IEEE*, (2014) pp. 272–277.
8. S. Hussain, P. K. Jamwal, M. H. Ghayesh and S. Q. Xie, "Assist-as-needed control of an intrinsically compliant robotic gait training orthosis," *IEEE Trans. Ind. Electron.* **64**(2), 1675–1685 (2017).
9. E. Burdet, G. Ganesh, C. Yang and A. Albu-Schäffer, "Interaction Force, Impedance and Trajectory Adaptation: By Humans, for Robots," **In**: *Experimental Robotics* (O. Khatib, V. Kumar and G. Sukhatme, eds.), Springer Tracts in Advanced Robotics, vol. 79, (Springer, Berlin, Heidelberg, 2014) pp. 331–345.
10. H. Mehdi and O. Boubaker, "Stiffness and impedance control using Lyapunov theory for robot-aided rehabilitation," *Int. J. Social Robot.* **4**(1), 107–119 (2012).
11. Y. Li, S. Sam Ge and C. Yang, "Learning impedance control for physical robot–environment interaction," *Int. J. Control* **85**(2), 182–193 (2012).
12. M.-C. Chien and A.-C. Huang, "Adaptive impedance control of robot manipulators based on function approximation technique," *Robotica* **22**(04), 395–403 (2004).
13. D. A. Winter, *Biomechanics and Motor Control of Human Movement.* (Wiley, 2009).
14. N. Hogan, " Impedance control: An approach to manipulation: Part III applications," *J. Dynamic Syst., Meas. Control* **107**(2), 17 (1985).
15. S. Oh, E. Baek, S.-k. Song, S. Mohammed, D. Jeon and K. Kong, "A generalized control framework of assistive controllers and its application to lower limb exoskeletons," *Robot. Autonomous Syst.* **73**, 68–77 (2014).
16. N. Karavas, A. Ajoudani, N. Tsagarakis, J. Saglia, A. Bicchi and D. Caldwell, "Tele-impedance based assistive control for a compliant knee exoskeleton," *Robot. Autonomous Syst.* **73**, 78–90 (2014).
17. A. Taherifar, G. Vossoughi and A. Selk Ghafari, "Optimal target impedance selection of the robot interacting with human," *Adv. Robot.* **31**(8), 1–13 (2017).
18. J.-J. E. Slotine and W. Li, Applied *N*onlinear *C*ontrol (*N*o. 1). (Prentice-Hall, Englewood Cliffs, NJ, 1991).
19. A.-C. Huang and M.-C. Chien, *Adaptive Control of Robot Manipulators: A Unified Regressor-free Approach.* (World Scientific, 2010).

20. M. Sharifi, S. Behzadipour and G. Vossoughi, "Nonlinear model reference adaptive impedance control for human–robot interactions," *Control Eng. Practice* **32**, 9–27 (11//2014).
21. T. Tsuji and Y. Tanaka, "Bio-mimetic impedance control of robotic manipulator for dynamic contact tasks," *Robot. Autonomous Syst.* **56**(4), 306–316 (2008).
22. C.-Y. Kai and A.-C. Huang, "A regressor-free adaptive controller for robot manipulators without Slotine and Li's modification," *Robotica* **31**(07), 1051–1058 (2013).
23. R. Desai and H. Geyer, "Robust Swing Leg Placement under Large Disturbances," *Proceedings of the Robotics and Biomimetics (ROBIO), 2012 IEEE International Conference on IEEE*, (2012) pp. 265–270.
24. R. Desai and H. Geyer, "Muscle-reflex Control of Robust Swing Leg Placement," *Proceedings of the Robotics and Automation (ICRA), 2013 IEEE International Conference on IEEE*, (2013) pp. 2169–2174.
25. S. Song, R. Desai and H. Geyer, "Integration of an Adaptive Swing Control into a Neuromuscular Human Walking Model," *Proceedings of the Engineering in Medicine and Biology Society (EMBC), 2013 35th Annual International Conference of the IEEE*, (2013) pp. 4915–4918.